**PAPER • OPEN ACCESS**

# First experimental confirmation of island SOL geometry effects in a high radiation regime on W7-X

View the article online for updates and enhancements.

# First experimental confirmation of island SOL geometry effects in a high radiation regime on W7-X

**V.R. Winters**[1,*] , **F. Reimold**[1] , **Y. Feng**[1] , **D. Zhang**[1] , **V. Perseo**[1] , **E.R. Flom**[2] ,
**F. Henke**[1], **D.M. Kriete**[3] , **N. Maaziz**[1], **G. Partesotti**[1] , **M. Jakubowski**[1] , **R. König**[1] ,
**M. Krychowiak**[1] , **K.J. Brunner**[1] , **J. Knauer**[1] , **K. Rahbarnia**[1] and the W7-X Team[a]

[1] Max-Planck-Institut für Plasmaphysik, 17491 Greifswald, Germany
[2] University of Wisconsin—Madison, Madison, WI, United States of America
[3] Auburn University, Auburn, AL, United States of America

E-mail: victoria.winters@ipp.mpg.de

CrossMark

## Abstract

This work characterizes the detachment behavior and radiation characteristics of the low iota
configuration in the Wendelstein 7-X (W7-X) stellarator. The island scrape-off layer (SOL) of
the low iota has a poloidal mode number of six islands surrounding the last closed flux surface
(LCFS). The island geometry of the low iota configuration is significantly different from that of
the standard magnetic field configuration, whose detachment characteristics have already been
described in previous work (Schmitz *et al* 2021 *Nucl. Fusion* **61** 016026, Jakubowski *et al* 2021
*Nucl. Fusion* **61** 106003, Feng *et al* 2021 **61** 086012). Experimental results show that the
radiation pattern in the low iota configuration is starkly different from that of the standard
magnetic field configuration, with radiation concentrated at the island SOL O-points, rather than
the X-points. Additionally, this O-point localized radiation pattern is associated with unstable
detachment, with both radiation oscillations in experiments and the lack of a self-consistent
plasma solution at high radiated power fraction in EMC3-Eirene simulations. EMC3-Eirene
simulations are used to understand the radiation distribution. It was found that the O-point
localized radiation arises first from local impurity accumulation near the parallel flow
stagnation, which is located close to the geometrical center of the island (the "O-point"). Local
cooling in this region leads to plasma condensation in the islands in the closest magnetic
connection to the divertor target plates. The heat source to this region of the island, which is
thermally isolated from the upstream heat source in terms of parallel transport, must arise via
perpendicular heat transport. This heat source is expected to be large for the low iota
configuration due to its very small internal island field line pitch. This work highlights the
importance (complementary to previous work, e.g. Feng *et al* (2005 *Nucl. Fusion* **45** 89), Feng
*et al* (2011 *Plasma Phys. Control. Fusion* **53** 024009)) of the internal island field line pitch not
only on the radiation pattern but also the detachment performance of the island divertor.

---

## 1. Introduction

The island divertor concept, employed in the Wendelstein 7-X (W7-X) stellarator, has already demonstrated successful detachment in the standard magnetic field configuration [1, 2], even over long timescales [3], during the third W7-X experimental campaign (OP1.2b). However, the detachment performance of other magnetic field configurations, particularly those with different island geometry, has not yet been as well-characterized. The predecessor to W7-X, W7-AS, has shown that the stable detachment operation depends strongly on the island scrape-off layer (SOL) geometry [4]. Therefore, it is crucial to map out and understand the differences in detachment performance with the island geometry in W7-X. These differences can then be taken into consideration in further optimization of the island divertor concept.

In the fourth W7-X experimental campaign (OP2.1), detachment was investigated in different island geometries. For one of these configurations (known as 'low iota'), intense radiation was observed at the island O-point, unlike previous observations in the so-called 'standard' magnetic field configuration. The standard configuration was characterized by intense radiation near the island X-points [1, 5]. Additionally, at high radiated power fractions, stable detachment was not achieved in the low iota configuration. This paper aims to describe the detachment behavior of the low iota configuration and explore how differences in its island geometry, in comparison with the standard configuration, may contribute to its distinct radiative characteristics. Section 2 will introduce the main island SOL geometry differences between the low iota and standard configurations and section 3 will provide an overview of the experimental observations. To help interpret the experimental observations, EMC3-Eirene [6] modeling is used. Section 4 will describe the simulation set-up, and section 5 will present experimental-model comparisons. Finally, Sections 6 and 7 will discuss the reasons for the observed radiation distribution in low iota.

## 2. The island divertor configuration space of W7-X

A 3D image of the W7-X divertor geometry is plotted in figure 1. W7-X exhibits five-fold symmetry, with each of the five toroidally identical modules containing two discontinuous divertor target plates. One divertor is located on the upper half of the machine and the other on the lower half. All ten divertor targets are plotted in figure 1(*a*) in dark gray. The targets intersect magnetic islands that form naturally on a rational surface at the plasma edge. An example of how these target intersections form the W7-X island SOL is plotted in figures 1(*b*) and (*c*) for the low iota configuration. Figures 1(*b*) and (*c*) show the target-to-target magnetic connection length pattern

for toroidal angles $\varphi = 0°$ and $\varphi = 36°$ (indicated by gray squares in figure 1(*a*)). Six islands are seen to surround the LCFS (more accurately, a single island which wraps poloidally around the LCFS six times). Of these islands, two are in close magnetic connection to the plasma-target interaction region (strike-line) at $\varphi = 36°$. These two islands correspond to the upper divertor in toroidal module 1 ($\varphi = -36 - 36°$) and the lower divertor in module 2 ($\varphi = 36 - 108°$) and are marked in figures 1(*b*) and (*c*) as red and blue dots, respectively. Note: there is no divertor target plate at $\varphi = 36°$, however the islands marked by the red and blue dots are in short magnetic connection (less than 1/10th of a toroidal turn) to divertor target plates.

W7-X was designed for magnetic flexibility. Therefore, the divertor structures are not tailored to any single magnetic field configuration. Rather, they conform to the basic flux surface shape of the device. The SOL geometry varies considerably with magnetic field configuration. W7-X operates within a magnetic configuration space where the edge rotational transform at the island-forming surface can be $\iota = 5/6$, $\iota = 5/5$ and $\iota = 5/4$ [7]. Poincare maps for paradigmatic magnetic configurations utilizing these 3 choices for edge rotational transform at the bean-shaped cross-section (toroidal angle $\varphi = 0°$) are plotted in figure 2. For the low iota ($\iota = 5/6$) and high iota ($\iota = 5/4$) configurations a 6 and 4 island chain poloidally surrounds the LCFS, respectively. For the standard ($\iota = 5/5$) configuration, five independent magnetic islands surround the LCFS. The Poincare plots in figure 2 represent the island SOL configurations assuming vacuum fields.

The open field lines in the island SOL move poloidally around the island in accordance with the internal island field line pitch, $\Theta$. The internal island field line pitch is defined as the ratio of the poloidal displacement of the field line per arc length within the island measured with the axis located at the island O-point. The low shear design of W7-X results in a relatively small island field line pitch, with $\Theta$ on the order of 0.001. The ratio of parallel to perpendicular transport in the island SOL scales as $\sim \Theta^2$ [8], indicating that the transport characteristics are highly sensitive to this parameter. Because of the small SOL field line pitch of the W7-X islands compared to a tokamak ($\Theta \sim 0.1$), the weight of perpendicular transport in the stellarator island divertor becomes comparable to that of parallel transport [8] over the majority of the operational space. However, because of W7-X's flexible magnetic geometry, it is possible to tune the ratio of parallel to perpendicular transport of the island divertor by modifying the internal rotational transform of the island. $\Theta$ is a function of multiple geometric parameters of the machine, with the maximum value within the island determined by [9]:

$$\Theta = \frac{r_i \iota' a}{R}. \tag{1}$$
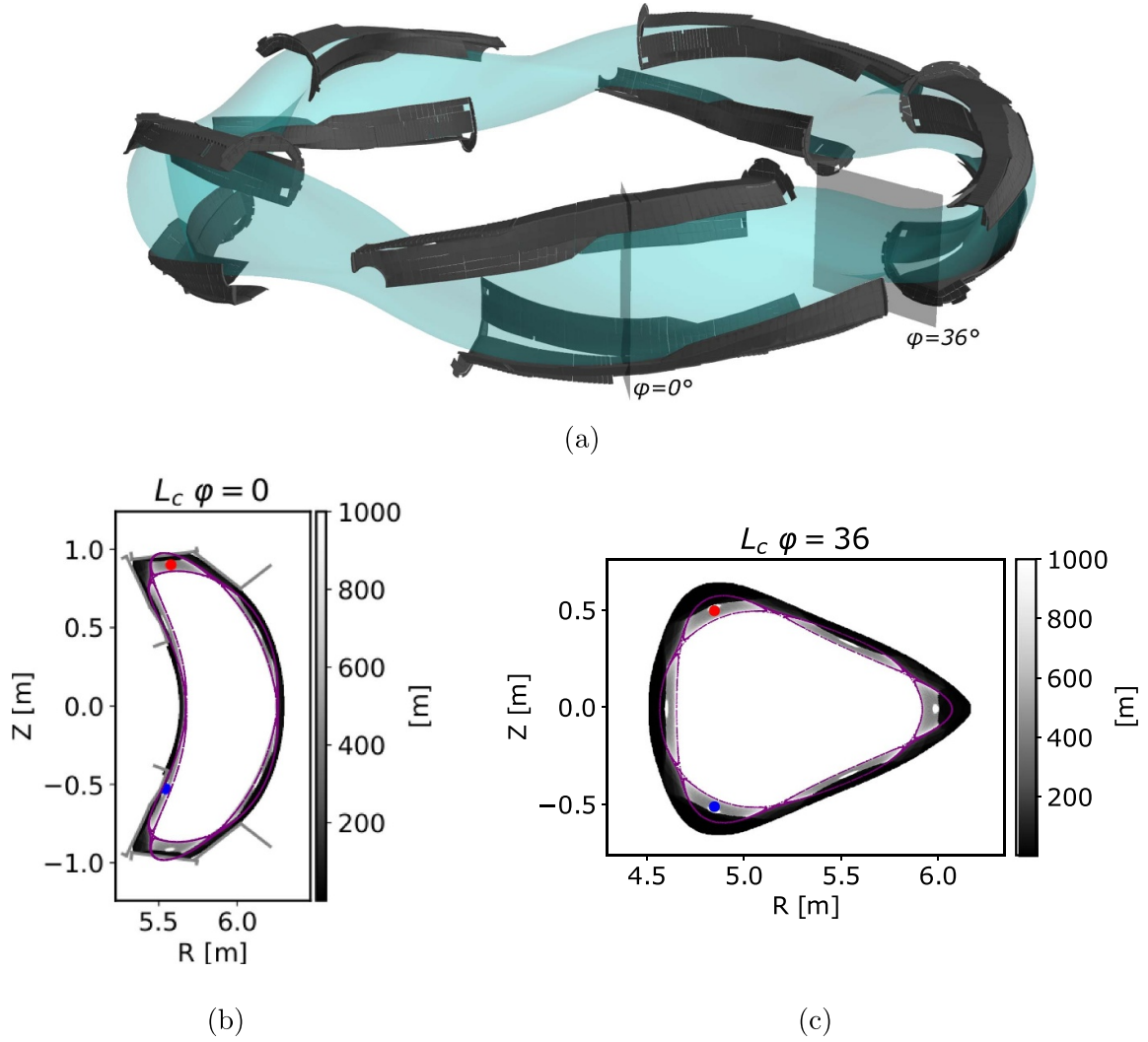
**Figure 1.** (*a*) The divertor geometry of W7-X. W7-X has five identical toroidal modules, with each module containing one upper and one lower divertor, plotted in dark gray. The LCFS contour is plotted in light blue. In black are two poloidal cuts at $\varphi = 0^\circ$ and $\varphi = 36^\circ$, respectively. The connection length plots for these two contours are plotted in (*b*) and (*c*), respectively. The island that connects to the upper horizontal divertor target plate in toroidal module 1 is marked with a red dot in both connection length plots. The island that connects to the lower horizontal divertor target plate in toroidal module 2 is marked with a blue dot. These two islands are closest magnetically to the plasma strike lines at $\varphi = 36^\circ$ (the triangular plane).

In equation (1), $\iota'$ is the shear at the resonant surface and $a/R$ is the machine aspect ratio. $r_i$ is the radial width of the island defined as [10]:

$$r_i = 2\sqrt{\frac{Rb_{rm}}{\iota' m}} \qquad (2)$$

where $b_{rm}$ is the magnitude of the radial resonant field component and $m$ is the poloidal mode number of islands [9]. Putting together equations (1) and (2) leads to the following equation for the internal island field line pitch:

$$\Theta = 2a\sqrt{\frac{\iota' b_{rm}}{Rm}}. \qquad (3)$$

Equation (3) shows the important parameters that have an effect on $\Theta$ and hence the transport properties of the island

divertor. Higher shear (within the low shear limits of maintaining good island flux surfaces and avoiding low-order resonances in the confinement region) and a higher resonant field component at the resonant surface will increase $\Theta$ and thereby the weight of parallel transport. A smaller poloidal number of islands will also increase the weight of parallel transport. As expected from equation (3), low iota ($m = 6$, with lowest shear) has the smallest internal island field line pitch, while high iota ($m = 4$, with highest shear) has the largest internal island field line pitch within the magnetic configuration space.

A set of island control coils has been installed in W7-X [7] that can also be used to tune the internal island field line pitch. The control coils change $\Theta$ primarily by changing the radial resonant field component $b_{rm}$ and therefore the island size. For example, the nominal island width in the standard configuration is $r_i = 7\,\text{cm}$. Using a controlled coil current $I_{cc} = 2.5\,\text{kA}$,
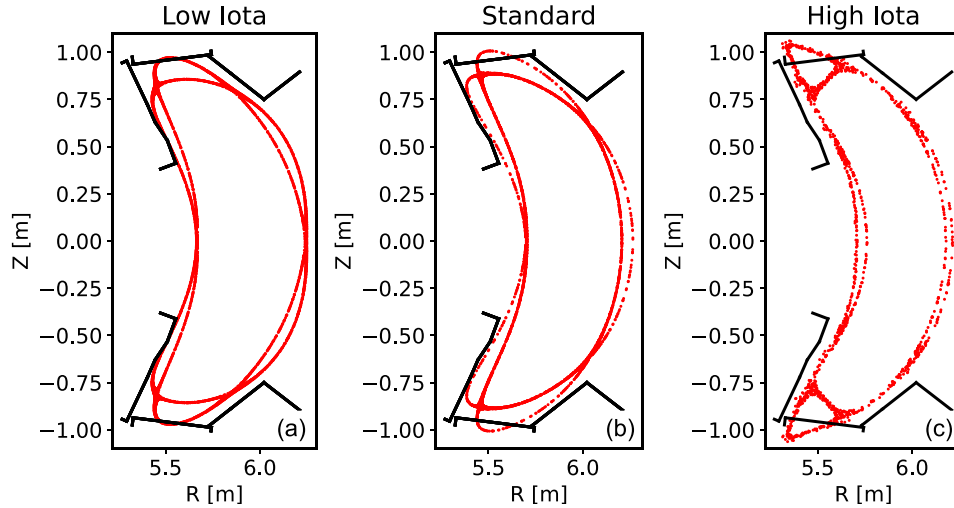
**Figure 2.** Poincare plots of the island geometry for (*a*) the low iota configuration (*b*) the standard configuration and (*c*) the high iota configuration in the bean shaped cross section ($\varphi = 0^\circ$). Low iota exhibits an $m = 6$ island chain surrounding the LCFS, standard exhibits an $m = 5$ island chain, and high iota an $m = 4$ island chain.

the island width can be increased to approximately 10 cm. Conversely, the application of $I_{cc} = -1$ kA shrinks the island size to approximately 5 cm. Between these two control coils current values, the ratio of parallel to perpendicular transport in the standard configuration can be modified by about a factor of 4, based on the simplified stellarator SOL model outlined in [8].

The sensitivity of the SOL transport properties to the island geometry, based on simplified models of the stellarator SOL [8], suggests that there is significant room for divertor performance optimization. For example, it is hypothesized that the high recycling regime observed on W7-X [11] but not at W7-AS [12] or in the open divertor of LHD [13] is due to the higher field line pitch of the W7-X islands. On the other hand, the longer connection length and increased weight of perpendicular transport is beneficial for the reduction of the parallel ion thermal force acting on the impurities [8]. In fact, EMC3-Eirene modeling predicts that under typical operating conditions, the impurity transport in the W7-X island SOL in the standard configuration is dominated by the ionization length and perpendicular transport mechanisms [14]. With both impurity transport and density build-up expected to be sensitive to island geometry, it is consequently expected that detachment performance and radiation distribution are also affected. First experimental evidence of such effects on radiation distribution will be presented in the following section.

## 3. Overview of experimental observations

Plotted in figure 3 are overview parameters of representative detachment programs for both the low iota (black and red) and standard (blue) magnetic field configurations. The low iota program plotted in black (20230125.18) is a representative program for intrinsic detachment using carbon radiation, while the program plotted in red (20230125.43) is representative of

a neon-seeded program. The experimental program plotted in blue (20230209.30) is typical behavior of intrinsic detachment in the standard magnetic field configuration. The total input heating power, supplied by electron cyclotron resonance heating (ECRH), is plotted in (a) as solid lines. Programs 20230125.18 and 20230209.30 have the same input heating power (3 MW), while program 20230125.43 has a slightly higher input heating power (4 MW). The total radiated power, measured by the bolometer [5], is plotted additionally as dotted-dashed lines. The line integrated density measured by the interferometer [15] is plotted in (b) and the diamagnetic energy [16] is plotted in (c). All experiments are performed post-boronization, which substantially (more than one order of magnitude) reduces the oxygen content of these plasmas [17].

Several key differences in the detachment behavior of the low iota versus the standard configuration are evident in the overview parameters of figure 3. Firstly, in the low iota configuration, the radiated power, $P_{rad}$, is maintained at a relatively low level until it reaches around 50%–60% of the input ECRH power. Upon reaching this level, a rapid transition to $P_{rad}$ values around 100% of the input power occurs. This phenomenon occurs both in the density ramp experiment (20230125.18), despite the slow increase, and with nitrogen seeding (not shown). However, experiments utilizing neon seeding (20230125.43) demonstrate greater controllability of the $P_{rad}$ level, maintaining control up to a radiated power fraction of 75%–80%. Upon the transition to high $P_{rad}$ in the low iota programs, a significant drop in the diamagnetic energy is observed. This behavior for both intrinsic and impurity-seeded plasmas is in stark contrast to the detachment behavior observed in the standard magnetic field configuration. As an example, in program 20230209.30, intrinsic detachment in standard configuration is achieved via a density ramp performed similarly to 20230125.18. However, unlike program 20230125.18, the $P_{rad}$ signal in this configuration increases
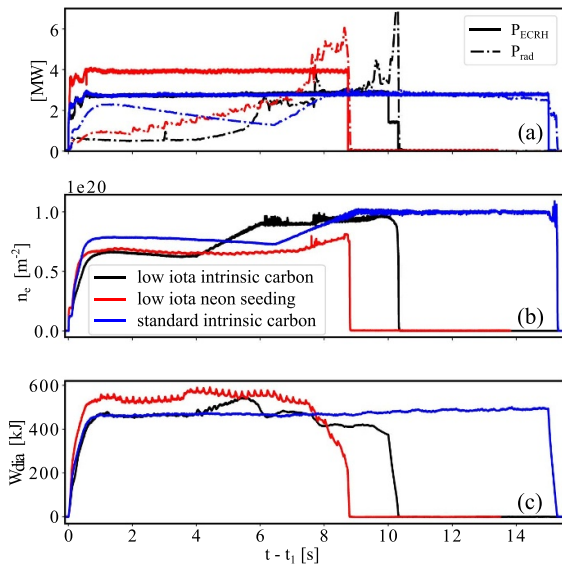
**Figure 3.** Representative overview plots for detachment in low iota configuration via intrinsic carbon radiation (20230125.18, in black) and neon seeding (20230125.43, in red) compared with detachment in the standard configuration using intrinsic carbon radiation (20230209.30, in blue). Both 20230125.18 and 20230209.30 use the same input heating power, although the heating power is not clearly visible for 20230125.18.

proportionally to the density ramp, and a smooth transition to 100% radiated power fraction is observed without a corresponding decrease in the diamagnetic energy. The initial higher value and the corresponding decrease of $P_{rad}$ in program 20230209.30 was caused by Argon injection that was intended to be traced (for diagnostic purposes) but was larger than expected.

After the transition to the high radiation regime, another noticeable difference between the low iota and standard configuration is evident: low iota experiences large oscillations both in the radiated power fraction and the line integrated density that is generally not seen in the standard configuration. However, the focus of this paper is to characterize the radiation distribution prior to the detachment instability and therefore the physics behind this difference is left to future work.

Detailed detachment characterization is difficult for these experimental programs because neither the divertor Langmuir Probes nor the H-alpha cameras were available for the OP2.1 experimental campaign (the divertor probes came online only in the final week of operation). On top of this, the data from the IR cameras is of poor quality, due to low signal to noise ratio. Therefore, detailed detachment characterization (e.g. the $f_{rad}$ value upon which the particle flux rolls over) is left to the upcoming experimental campaign, where both the Langmuir Probes and H-alpha cameras are expected to be routinely operational. In this work, we will focus primarily on studying the radiation behavior. In particular, the radiation behavior of the low iota configuration right before the radiation becomes unstable.

Examining the radiation distribution in more detail reveals additional variations between the two magnetic configurations. Previous work has shown that the radiation of the standard configuration is relatively evenly distributed around the SOL, but concentrated near the island X-points [1, 5] at high radiated power fraction. Tomographic reconstructions of the radiated power distribution from the bolometer diagnostic [5] of 20230209.30 confirm this behavior, as plotted in figure 4(*a*). However, reconstructions of the radiated power distribution in the low iota configuration, figure 4(*b*), reveal a significantly different radiation pattern. Firstly, the radiation pattern appears to be much more localized than the one for the standard configuration, concentrated on 2 small regions both on the upper and lower half of the machine. On the upper half of the machine, the radiation peaks strongly in the island O-point region on the upper inboard side. On the lower half, the radiation appears to be concentrated primarily between two islands, but also with a lower intensity region near the island O-point region. The differences in the radiation between the upper and lower half of the machine represent a significant up/-down asymmetry that has been observed experimentally also for other magnetic configurations [5] and may be attributable to drift effects [18, 19]. Further work is required to determine the exact cause of this asymmetry for the low iota magnetic configuration.

The O-point localized radiation is also observed in the Coherence Imaging Spectroscopy (CIS) system viewing the C-III 465 nm line radiation in one of the lower divertors (specifically, in toroidal module 3) [20], as well as in multiple impurity lines measured by the visible divertor spectroscopy system, which views one of the upper divertors [21]. Images of the C-III emission intensity from the CIS divertor viewing system for 20230125.18 are plotted in figure 5. Figure 5(*a*) is taken at low radiated power fraction ($f_{rad} \approx 20\%$), near the beginning of the program, while (b) corresponds to a time point where $f_{rad}$ is around 60% of the input heating power (right before the radiation becomes unstable). The CIS system has a top-down view of the horizontal divertor target plate, in a location that views a portion of the strike-line. Figure 5(*c*) shows the radiation from figure 5(*b*) superimposed on the viewing geometry of the system. The solid white lines in (c) correspond to the projected locations of the island O-points, while the dashed white lines correspond to the projected locations of the island X-points in the low iota configuration. In figure 5(*a*), the main C-III radiation zone corresponds to the strike-line on the divertor (labeled A in the figures). However, upon reaching $f_{rad} \approx 60\%$, the main radiation zone shifts to the location of the island O-point, away from the plasma strike line (labeled B in the figures). The narrow stripe of radiation that is seen between the vertical and horizontal targets for both the low and high radiation case is known to be a reflection from the stainless steel panel behind the divertor. The rest of the viewing area is believed to be minimally affected by reflections in the visible wavelengths because the divertors are made of graphite, a material with relatively low reflectivity.

The differences in the detachment behavior of the low iota and standard configurations are reminiscent of observations
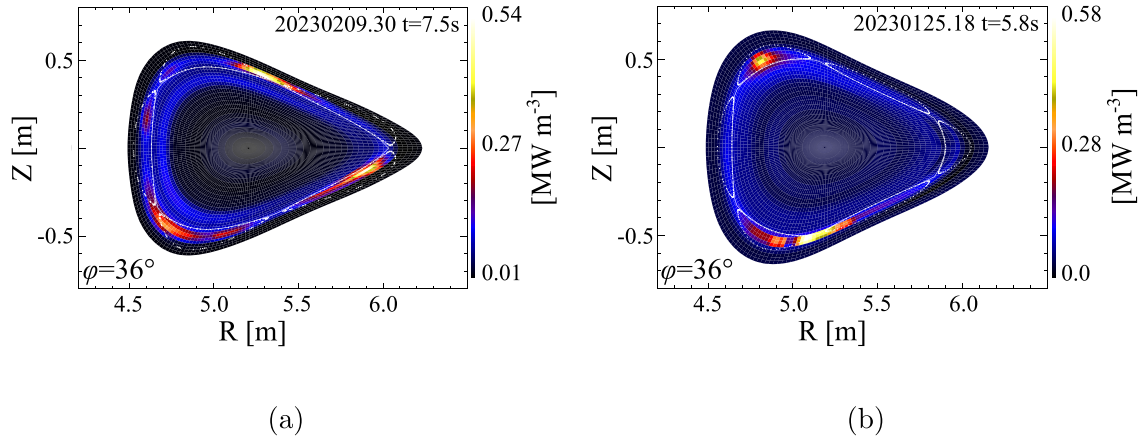
**Figure 4.** Tomographic reconstructions of the radiated power distribution from the bolometer diagnostic for (*a*) 20230209.30 at $t = 7.5$ s (standard configuration $f_{rad} \approx 90\%$) and (*b*) 20230125.18 at $t = 5.8$ s (low iota configuration $f_{rad} \approx 60\%$). The LCFS and island separatrix are plotted as white dots. The bolometer observes in the triangular plane, which is located at $\varphi = 36°$ (and stellarator symmetric locations).
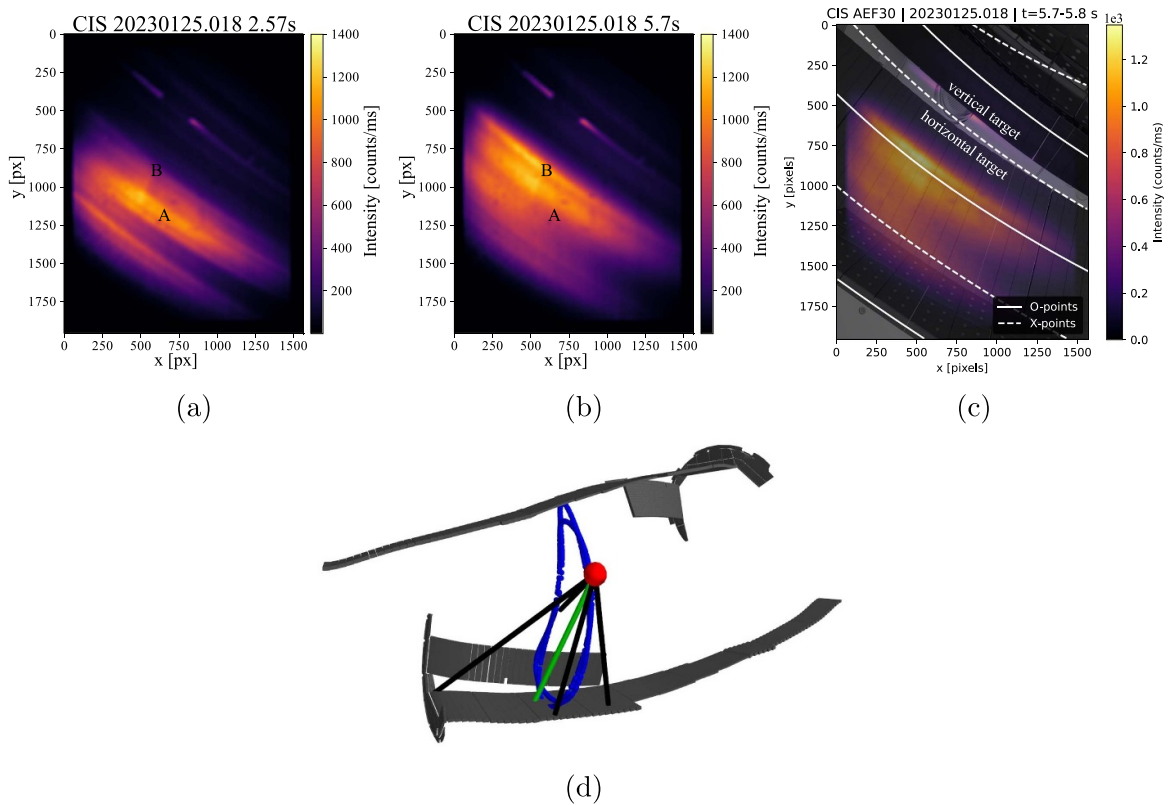


**Figure 5.** C-III (CWL 465 nm) emission intensity as measured by the CIS camera viewing the divertor targets at (*a*) 2.57 s (low $f_{rad}$) and at (*b*) 5.7 s (high $f_{rad}$) for program 20230125.18. (*c*) superimposes the emission from (*b*) on the CAD geometry of the divertor target plates. In (*c*), the locations of the O- and the X-points for the low iota configuration projected onto the lines of sight are plotted as solid and dashed white lines, respectively. A high intensity emission band near the island O-point region above the horizontal divertor target is observed at high $f_{rad}$. (*d*) Shows a 3D view of the CIS camera view. The divertor target plates are plotted in gray, the camera position is plotted as a red dot. The viewing area is enclosed in the four black lines, with the center viewing area plotted in green. A poincare map near the center viewing area of the camera is plotted in blue.

made on W7-AS, the predecessor to W7-X. In W7-AS, it was observed that small island sizes and/or islands with small internal island field line pitch showed localized divertor radiation, whereas larger islands and/or islands with larger internal island field line pitch exhibited a more evenly distributed radiation pattern [4]. Additionally, for the former, the detachment was also unstable [4]. Although the localized divertor radiation pattern for the small island sizes or internal field line pitch was not fully understood, it is believed that the increased weight of the cross-field transport from the smaller internal

island field line pitch resulted in the width of the heat flux channel becoming comparable to the island size itself [22]. A consequence of such a phenomenon is that a considerable fraction of the power entering the SOL (from the outboard side) would be intercepted by the divertor plates before it reached the inboard side (where flux expansion of the islands favored radiation). This process could lead to the localized radiation pattern in front of the divertor [22].

However, the island geometry of W7-X is considerably different from that of W7-AS. Firstly, the W7-X island size is roughly twice that of the islands in W7-AS. This larger island size means that it is unlikely that the radiation layer is comparable to the island size. Additionally, differences between the W7-X and W7-AS low internal island field line pitch scenarios are seen experimentally. For example, in W7-AS, the divertor-localized radiation was localized to the X-point in simulation, rather than to the O-point as seen experimentally in W7-X. Therefore, it may be that the mechanism causing the localized radiation pattern in W7-X is different from that of W7-AS. To investigate this, plasma edge modeling using EMC3-Eirene is used to help elucidate the reasons for the O-point radiation observed in the low iota configuration.

## 4. EMC3-Eirene and simulation set-up

EMC3-Eirene is a 3D Braginskii plasma fluid solver coupled with the 3D kinetic neutral solver Eirene [23]. The code provides a self-consistent SOL plasma solution in steady-state [6]. Perpendicular transport is assumed to be anomalous with anomalous particle diffusion $D_\perp$ and heat diffusion $\chi_\perp$ coefficients given as input parameters. Impurities are treated as trace except for their radiation, which is coupled into the energy balance. Drift effects are outside the current capability of EMC3-Eirene and therefore not included. One-tenth of W7-X is simulated, assuming the stellarator symmetry of the device. Therefore, the effects of error-fields are not taken into account in the simulations.

There are various uncertainties (drifts, evolving bootstrap current, anomalous transport, error-fields...) involved when comparing the simulation results to experiment. For these simulations, plasma equilibrium effects (bootstrap current, finite beta) are not taken into account and therefore the vacuum field approximation is used. The finite beta of program 20230125.18 is unfortunately unknown due to missing profile data. However, previous simulation work using EMC3-Eirene simulations has indicated that while finite beta does have some effect on the plasma transport, the qualitative features of the radiation pattern remain quite similar [24]. Likewise, small shifts of the iota profile due to toroidal current (which shifts the islands in the same way as changes of planar coil current, used in [1]), also appear to not significantly change the qualitative behavior of the simulations [1]. With regards to error-fields, the low iota configuration is not resonant with the known 1/1 error field present in W7-X [25] and therefore its effects are expected to be negligible. The large remaining uncertainties are the choice of anomalous transport parameters and the effect of drifts.

Assessments of the anomalous transport coefficients in the standard configuration have been indicated from probe and heatflux width data that $D_\perp \sim 0.1 - 0.2 \, \mathrm{m^2 \, s^{-1}}$ [26, 27]. However, using these coefficients with the assumption $\chi_\perp = 3D_\perp$ generally results in a mismatch to upstream plasma temperatures [27]. Other simulation work for the standard configuration has found that $D_\perp = 0.5 \, \mathrm{m^2 \, s^{-1}}$ with $\chi_\perp = 1.5D_\perp$ appears to provide the best compromise in matching both upstream and downstream plasma parameters [28]. However, such studies, both experimentally and numerically, have not yet been performed for the island chain in the low iota configuration. As a starting point, $D_\perp = 0.5 \, \mathrm{m^2 \, s^{-1}}$ with $\chi_\perp = 1.5D_\perp$ is used. Sensitivity scans of the solution to these parameters, both for the main ions and the impurities, are used to determine the best match to experimental data and their results will be discussed in the next section.

The final uncertainty, the effects of drifts, cannot be handled by the EMC3-Eirene code and is therefore out of the scope of this paper. Previous experimental work has indicated that drifts play a substantial role in the plasma transport [18, 19]. Therefore, even with taking all other uncertainties into account, it is expected that a quantitative match to experimental data is impossible. Therefore, these simulations will aim to qualitatively match the behavior and trends of the experiments.

For all simulations discussed in this work, the power entering the SOL was set to be $P_{\mathrm{in}} = 5 \, \mathrm{MW}$, equally split between electrons and ions. This value deviates from the input heating power of the experiments because the starting set of simulations were performed prior to their execution. Although the input heating power of the experiments was $P_{\mathrm{in,tot}} = 3 \, \mathrm{MW}$, this difference in total heating power should not qualitatively affect the results shown in this work. To prove this, figure 6 provides a poloidal cross section of the radiated power distribution from 2 simulations: one with $P_{\mathrm{in,tot}} = 5 \, \mathrm{MW}$ (a) and one with $P_{\mathrm{in,tot}} = 3 \, \mathrm{MW}$ (b). All other input parameters were set to be equal ($n_{\mathrm{e,ibs}} = 5 \times 10^{19} \, \mathrm{m^{-3}}$, $f_{\mathrm{rad}} = 60\%$, $D_\perp = 0.5 \, \mathrm{m^2}$ $\mathrm{s^{-1}}$ and $\chi_\perp = 3D_\perp$). The simulation at lower total input heating power was scaled by a factor of 1.667 to account for the differences in magnitude of the total radiated power (1.8 MW versus 3.0 MW). The qualitative features of the radiation pattern between these two simulations remain the same: O-point radiation condensation occurs within the two islands located closest to the divertor, and with little radiation in the other islands.

A large amount of simulations were performed to study the effect of separatrix density, radiated power fraction, impurity species, and the choice of anomalous diffusion parameters. The exact input parameters for each simulation used in the following sections will be stated when they are introduced, but for clarity a summary of all simulations is documented in table 1. The initial energy of the impurity neutrals (intrinsic carbon) was set to $E_0 = 0.03 \, \mathrm{eV}$, with initial starting distributions the same as the distribution of the impinging main ion flux. In these simulations, the total carbon source is controlled by the
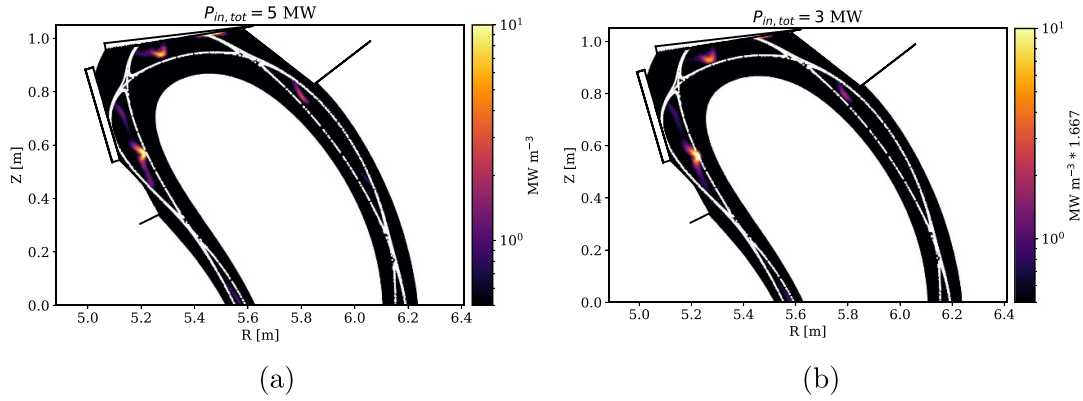
**Figure 6.** Two simulations where input parameters were completely identical except for the total input heating power. The radiation pattern for the $P_{in,tot} = 3$ MW simulation was scaled by a factor of 1.667 to account for differences of the total radiated power for the two simulations.

**Table 1.** A summary of the simulations that will be shown in this work. Each simulation will be referred to when it is used.
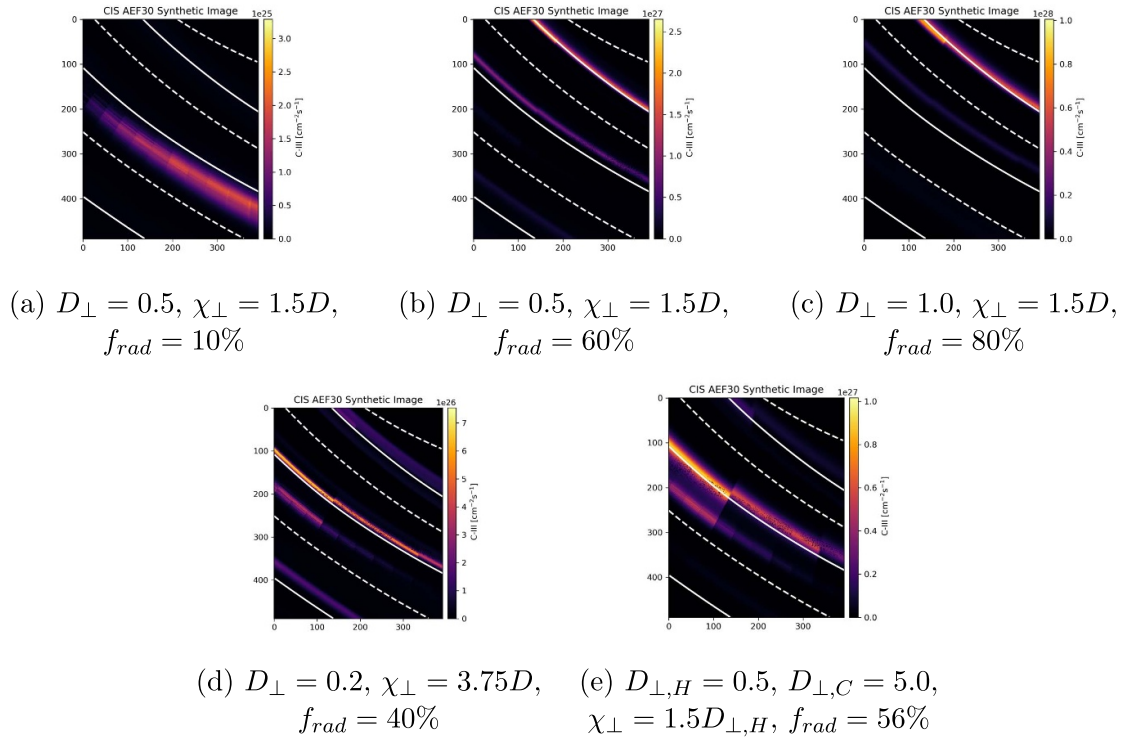
| Config | $D_\perp$ (m$^2$ s$^{-1}$) | $\chi_\perp$ | $n_{ibs}$ ($10^{19}$ m$^{-3}$) | Impurity source | $f_{rad}$ % | Remark |
|---|---|---|---|---|---|---|
| low iota | 0.5 | $1.50D_\perp$ | 5 | Carbon | 10 | |
| low iota | 0.5 | $1.50D_\perp$ | 5 | Carbon | 60 | |
| low iota | 1.0 | $1.50D_\perp$ | 5 | Carbon | 80 | |
| low iota | 0.2 | $3.75D_\perp$ | 5 | Carbon | 40 | |
| low iota | 0.5 | $1.50D_\perp$ | 5 | Carbon | 56 | $D_{\perp,C} = 5$ |
| low iota | 0.5 | $1.50D_\perp$ | 3 | Carbon | 15 | |
| low iota | 0.5 | $1.50D_\perp$ | 3 | Carbon | 60 | |
| low iota | 0.5 | $1.50D_\perp$ | 3 | Carbon | 60 | reconverged from $f_{rad} = 15\%$ case without Eirene |
| low iota | 0.5 | $1.50D_\perp$ | 5 | Carbon | 20 | |
| low iota | 0.5 | $1.50D_\perp$ | 5 | Neon | 60 | |
| standard | 0.5 | $1.50D_\perp$ | 5 | Carbon | 60 | |
| standard | 0.5 | $20.0D_\perp$ | 5 | Carbon | 60 | |
| standard | 0.5 | $1.50D_\perp$ | 5 | Carbon | 60 | with $I_{cc} = -1$ kA |

total radiated power requested in the simulation. Therefore, no effective sputtering yield is set. Rather, the total carbon content in the device is scaled up and down in order to match the total radiated power fraction. Controlling the carbon content with this method ensures that the simulation maintains a similar power balance as in the experiment. However, it is possible to take the ratio of the total carbon impurity source to the total recycling source as a mocked up 'sputtering coefficient'. For the case envisaged to be closest to the experiment ($f_{rad} = 60\%$, $n_{e,s} = 5 \times 10^{19}$ m$^{-3}$) this 'sputtering yield' is 4.9%. This value is in line with previous W7-X simulations that utilized a sputtering coefficient for carbon of around 4% [14, 29]. In the simulations where neon was used as the main radiator, the neon neutrals were also started with the same distribution as that of the impinging main ion flux. This is justified because neon is a highly recycling impurity in W7-X and therefore only gets pumped over long timescales. In the experiment, constant seeding of neon is not needed. Rather, short individual puffs are used to slowly raise the radiated power and results in the step-like shape of the radiated power signal for Program 20 230 125.43 shown in figure 3. As the neon recycles many times over, any information on the spatial localization of the

impurity from the puff itself gets lost. Using the same distribution as the main ion recycling flux is an approximation since it is not known if the recycled neon flux is deposited exactly in the same distribution as the main ions. However, since our simulations attempt to model the steady-state scenario, after the neon puff has been turned off with a constant $P_{rad}$ value maintained, we choose instead this assumption over introducing the neon impurities via an external puff from the seeding valve. This assumption also appears to be in line with previous experimental results, which have shown that neon seeding in W7-X resulted in equal heatflux reduction to all divertor target plates, rather than exhibiting a toroidal localization to the single divertor where the seeding valve was located [29].

## 5. Experiment-simulation comparison

Dedicated 1:1 comparisons of the radiation diagnostic measurements (CIS, bolometer) to simulation, using synthetic diagnostics for EMC3-Eirene [30–32], were performed for the low iota configuration. The comparison started with the initial simulation set described in section 4. However, based on

(a) $D_\perp = 0.5$, $\chi_\perp = 1.5D$, $f_{rad} = 10\%$

(b) $D_\perp = 0.5$, $\chi_\perp = 1.5D$, $f_{rad} = 60\%$

(c) $D_\perp = 1.0$, $\chi_\perp = 1.5D$, $f_{rad} = 80\%$

(d) $D_\perp = 0.2$, $\chi_\perp = 3.75D$, $f_{rad} = 40\%$

(e) $D_{\perp,H} = 0.5$, $D_{\perp,C} = 5.0$, $\chi_\perp = 1.5D_{\perp,H}$, $f_{rad} = 56\%$

**Figure 7.** Synthetic images of the CIS diagnostic viewing the divertor at (*a*) low radiated power fraction, (*b*) 60% $f_{rad}$ with $D_\perp = 0.5\,\mathrm{m^2\,s^{-1}}$ for all species, (*c*) 80% $f_{rad}$ with $D_\perp = 1.0\,\mathrm{m^2\,s^{-1}}$ for all species, (*d*) $f_{rad} = 40\%$ with $D_\perp = 1.0\,\mathrm{m^2\,s^{-1}}$ for all species and (*c*) 56% $f_{rad}$ with $D_\perp = 0.5$ and $D_\perp = 5\,\mathrm{m^2\,s^{-1}}$ for the main ions and impurities, respectively. At low $f_{rad}$, the radiation is primarily at the plasma strike line. However, at high $f_{rad}$ the primary radiation location moves to the island O-point region.

the level of qualitative agreement, the transport parameters were then tuned to best match the experiments. The synthetic diagnostics do not yet take into account signals from reflected light, which may provide additional discrepancies with the experiment on top of the physics limitations of EMC3-Eirene. However, at the toroidal location of the bolometer (stellarator-symmetric to $\varphi = 36°$) the entire vessel is covered in a layer of graphite tiles. Additionally, the bolometer measures mostly x-ray and UV radiation, which is not highly affected by reflections. In the case of the CIS (as discussed in section 3), only the small portion of the image between the vertical and horizontal targets (viewing stainless steel panels behind the divertor), contains lines of sight that end on a highly reflective surface. Therefore, we assume discrepancies due to light reflections are small in comparison to the missing physics in EMC3-Eirene.

At low radiated power fraction ($f_{rad} = 10\%$), the initial simulation set with $D_\perp = 0.5\,\mathrm{m^2\,s^{-1}}$ and $\chi_\perp = 1.5D_\perp$ shows relatively good agreement with the radiation pattern seen in experiment. An example from the synthetic CIS C-III radiation pattern is plotted in figure 7(*a*). As in figure 5(*c*), the solid white lines for all images plotted in figure 7 correspond to the projected island O-point locations for the low iota configuration, while the dashed white lines correspond to the projected X-point locations. Compared with figure 5(*a*), the main C-III radiation pattern remains concentrated in the same area, namely, the plasma strike-line. The synthetic image appears brighter in the lower right corner of figure 7(*a*) than in the

experiment. However, this arises at least partially because the experimental image is vignetted, a factor that is not considered in the synthetic images. The C-III radiation pattern at low radiated power fraction is relatively insensitive to the choice of anomalous transport coefficients because the C-III radiation remains strongly correlated to the impinging heat and particle flux location. As such, transport only plays a minor role in the radiation pattern, with the source being the dominating factor.

However, large deviations between the initial simulation set and the experiments occur with increased radiated power fraction ($f_{rad} > 40\%$). The synthetic reconstruction of the CIS camera for $f_{rad} = 60\%$ for the simulation set with $D_\perp = 0.5\,\mathrm{m^2}$ $\mathrm{s^{-1}}$ for all species is plotted in figure 7(*b*). The image shows two main radiation zones: the primary C-III radiation zone corresponds to the island O-point region above the vertical target (upper right portion of the images). A second radiation zone appears near the island O-point above the horizontal target plate. The radiation zones are also narrow in width. The pattern significantly differs from the experimental measurement, figure 5(*b*), which exhibits only one narrow radiation zone near the island O-point above the horizontal target plate. In addition, the experimental measurement shows a second, wider radiation zone directly below the narrow O-point radiation zone, and a third, lower intensity radiation zone near the X-point on the horizontal target plate (starting around $x = 0$px, $y = 1000$px).

The radiation pattern produced by EMC3-Eirene in the toroidal cross section of the bolometer also differs significantly
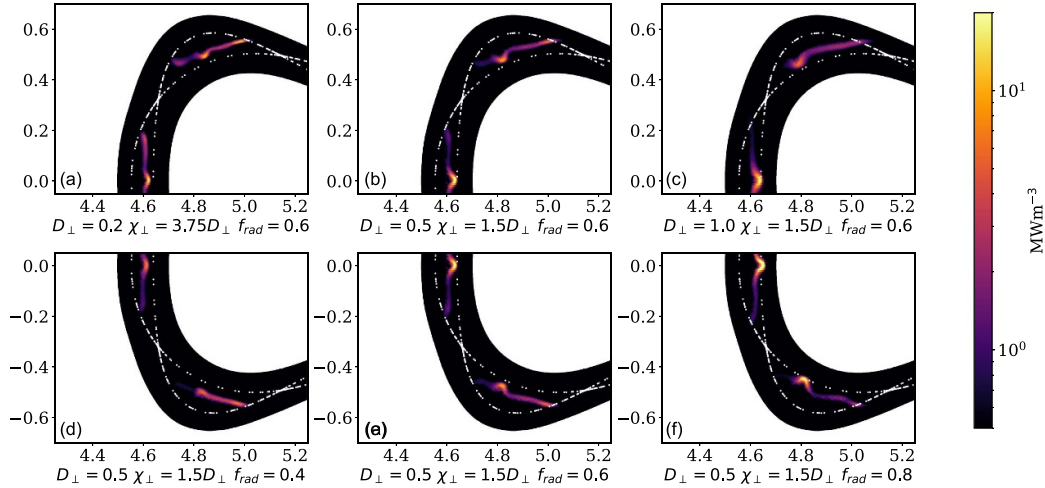
**Figure 8.** (*a*)–(*c*) Variations of the simulated radiation pattern distribution in the imaging plane of the bolometer with different choice of anomalous transport coefficients. (*d*)–(*f*) Variations of the radiation pattern distribution in the imaging plane of the bolometer with increasing radiated power fraction ($f_{\rm rad}$). In all cases, only two of the total six islands in the poloidal cross section are shown. The radiation in the upper (or lower island) is magnetically connected to the horizontal target, and the radiation coming from the inboard side island is magnetically connected to the vertical target. Because of the stellarator-symmetry assumption, all radiated power distributions in this imaging plane are up-down symmetric in the simulation.

from experiment when using the initial simulation set. Figure 8(*a*) shows the simulated impurity radiation in the toroidal cross section of the bolometer ($\varphi = 36°$) for the initial simulation set at $f_{\rm rad} = 60\%$. Although the location of the O-point radiation in the upper half of the image is reproduced, there is a strong band of radiation on the inboard-side island that does not appear in experiment. This band of radiation has a short parallel connection (1/10th of a toroidal turn) to the radiation band observed at the vertical target O-point in the CIS synthetic image (figure 7(*b*)).

An attempt at better matching the experimental conditions was therefore performed by tuning the anomalous transport coefficients, revealing that both the C-III and total radiation patterns are highly sensitive to the level of cross-field transport assumed. An analysis of many choices of anomalous parameters and radiation power fractions reveals two main trends:

(i) For a given $f_{\rm rad}$, increasing $D_\perp$ leads to an increased fraction of impurity radiation occurring in front of the vertical target.
(ii) For a given $D_\perp$, the larger the $f_{\rm rad}$, the larger the amount of radiation that occurs in front of the vertical target.

An example of the first trend can be seen in figures 8(*a*)–(*c*), where a scan of the anomalous parameters was performed, keeping all other parameters constant. In these figures, the radiation that is magnetically connected to the vertical target is located on the inboard-side island, with the radiation condensation region centered at $Z = 0.0$ m. From the smallest $D_\perp = 0.2 \, {\rm m}^2 \, {\rm s}^{-1}$ (for simplicity and to maintain realistic upstream temperatures $\chi_\perp$ is kept at $0.75 \, {\rm m}^2 \, {\rm s}^{-1}$, as in the $D_\perp = 0.5 \, {\rm m}^2 \, {\rm s}^{-1}$ simulations) to the largest $D_\perp = 1.0 \, {\rm m}^2 \, {\rm s}^{-1}$, a pronounced increase in the amount of radiation condensation at this inboard-side island is observed. A visualization of the

second trend is provided in figures 8(*d*)–(*f*). In this scan, the $D_\perp$ was kept constant, but the radiated power fraction was scanned from 40%–80%. A clear increase of the radiation magnitude is observed in both islands, however the magnitude of the radiation on the inboard side island significantly overtakes the radiation in front of the horizontal target (lower island) at around $f_{\rm rad} = 60\%$. This strong increase in the radiation on the inboard-side island is problematic for matching exactly the experimental radiation patterns that, as stated above and observed in figures 5(*b*) and 4(b), do not have this inboard-side radiation. Compared to the experiment, running a simulation at lower $f_{\rm rad}$ (40% rather than the 60% shown in figures 5(*b*) and 4(b)) at $D_\perp = 0.2$ largely avoids the radiation condensation in front of the vertical target, as shown in figure 7(*d*). Alternatively, setting the $D_\perp$ for the carbon impurity only to very high values $D_{\perp,C} = 5 \, {\rm m}^2 \, {\rm s}^{-1}$ can also remove the radiation condensation in front of the vertical target, as visualized in figure 7(*e*). However, there is no physics motivation for this choice of anomalous diffusion coefficient and although it appears to better match the CIS camera view, it then differs from the bolometer radiation distribution pattern (not shown). The discontinuities observed in the C-III radiation pattern in figure 7(*e*) arise from the finite grid resolution of the simulation. To reduce computational time, portions of the plasma simulation grid cells in EMC3 are merged toroidally. Close to the divertor target plate, no toroidal merging of cells is performed, leading to a grid resolution of approximately 1° toroidally. In these simulations (only in locations further away from the targets, closer to the LCFS), toroidal merging is performed such that the resolution is 6° toroidally. In the extreme case of the very large carbon diffusion coefficient, it is likely that the 6° toroidal resolution near the LCFS is not fine enough to avoid these artifacts.

After consideration of the above scans of radiated power fraction and anomalous input parameters, we determine that it could generally be the case that lower anomalous transport coefficients ($D_\perp = 0.2 \, \mathrm{m^2 \, s^{-1}}$) provides closer agreement with experiment by avoiding radiation condensation in front of the vertical target for a larger range of radiated power fractions (up to 40%). However, at $f_{\mathrm{rad}} = 60\%$, even at these low diffusion coefficients, the simulations show some amount of radiation in front of the vertical target (figure 8(*a*)). The origin for the radiation in front of the vertical target is not yet clear. However, recent results using simplified EMC3-Eirene modeling (not including impurity transport) [33] have indicated that this radiation condensation (in front of both the vertical and horizontal target) disappears when blocking neutral sources from entering the 'O-point' area in front of the horizontal target. Thus, it is likely that the radiation in front of both the horizontal and vertical target are connected to neutral sources in front of the horizontal target. However, when tracing a field line starting from the peak radiation in front of the vertical target, it appears to not be on the same field line as the peak radiation in front of the horizontal target. Future work is planned to study multiple flux tubes to understand how the radiation in front of the two divertors are related. However, with the missing physics in the simulations an exact match to the 3D radiation pattern is not expected. Regardless of such mismatches, it is clear that no matter the choice of anomalous transport parameters, the radiation pattern in front of the horizontal target condenses at the island O-point region rather than near the X-points. This robust tendency, both in experiment and modeling, can therefore be investigated numerically to understand its origin.

## 6. Results: island geometry's role in the O-point radiation pattern

In the previous sections, the unique aspect of detachment in the low iota configuration (island O-point localized radiation) has been introduced, which is suspected to be caused by the small field line pitch and the resulting large ratio of perpendicular to parallel heat transport. Now, its general access conditions will be investigated on a broader basis.

There are two ways to increase the relative weight of perpendicular heat transport in the simulations:

(i) Increase the anomalous heat diffusion coefficient, $\chi_\perp$, keeping all other terms constant.
(ii) Decrease the internal island field line pitch, $\Theta$.

In order to demonstrate the general validity of the above hypothesis, we use the standard island configuration here instead of the low-iota island chain. The former is ideal for this numerical experiment since X-point radiation is the standard radiation picture known to date. In the following, we will show how the O-point radiation pattern can be achieved by adjusting the above two parameters. Three simulations are performed, all with the same inner boundary density $n_{\mathrm{ibs}} = 5 \times 10^{19} \, \mathrm{m^{-3}}$ and $f_{\mathrm{rad}} = 60\%$ coming from carbon. The first simulation

uses the typical choice of anomalous transport coefficients $D_\perp = 0.5$, $\chi_\perp = 1.5 D_\perp$. The second simulation increases the anomalous heat transport coefficient only, with $\chi_\perp = 20 D_\perp$. Finally, the third simulation uses the same anomalous transport coefficients as the first simulation, however the island geometry is modified to have a lower internal island field line pitch. This is achieved by adding $-1 \, \mathrm{kA}$ of island control coil current, as discussed in section 2. The radiation patterns for these three simulations at a toroidal angle $\varphi = 10°$ are plotted in figure 9.

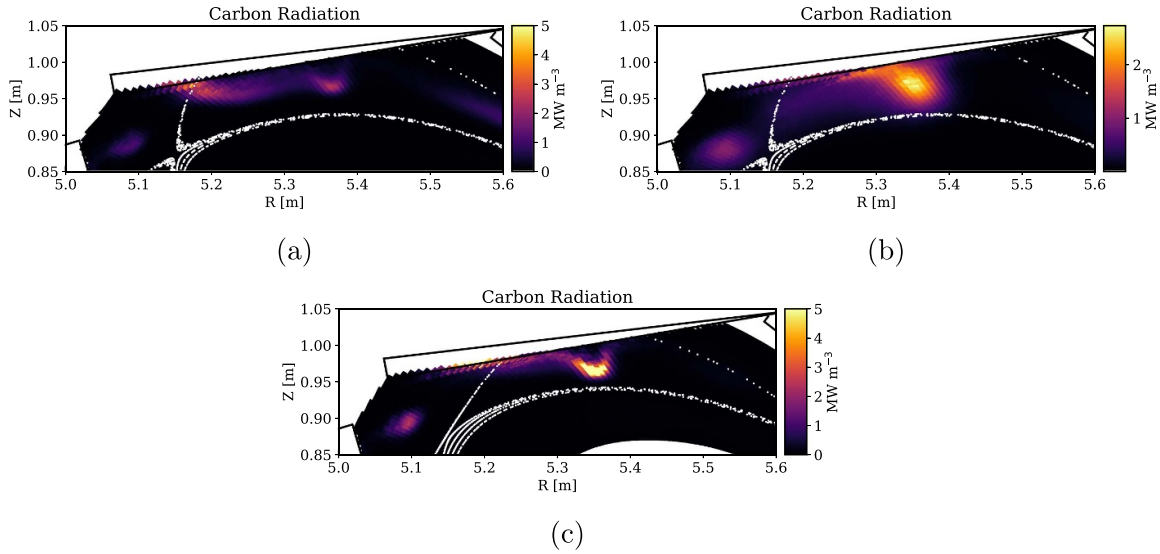Under the standard transport assumptions at $f_{\mathrm{rad}} = 60\%$ (figure 9(*a*)), the radiation has only started to lift off of the target and has the typical distribution of the initial radiation that eventually passes through the X-point with further increases in radiation level (more examples of this typical distribution can be found in [1]). There are two radiation regions, one near the location where the island separatrix intersects the divertor target (the strike-line), and one near the island O-point. However, the magnitude of the O-point radiation is smaller than that near the plasma strike-line. With an increase in $\chi_\perp$ (figure 9(*b*)) or a decrease in the internal island field line pitch (figure 9(*c*)), the radiation pattern significantly changes. In particular, both figures 9(*b*) and (*c*) now exhibit primarily radiation near the island O-point, similar to that of the low iota configuration. These results confirm that it is the increased amount of perpendicular transport that results in the O-point localized radiation pattern. We turn our efforts now to understanding a possible trigger for the localized radiation pattern. This analysis will once again focus on the low iota configuration.

### 6.1. 3D effects on the radiation distribution

It is clear from both experiment (figure 4(*b*)) and modeling that the island O-point localized radiation pattern is not present in all islands surrounding the LCFS in the low iota configuration. This observation indicates that the O-point radiation is not a helically-closed band, but rather arises from local 3D effects. In particular, we see that the islands with O-point radiation in both experiment and modeling are those that are located in closest magnetic proximity to the divertor strike-line (figure 1(*c*), shown as red and blue dots, respectively). This implies that the radiation arises in part due to impurity and/or ionization source effects near the recycling surface.

To gain deeper insight into how source effects play a role in the radiation pattern, a simulation with an inner boundary density $n_{\mathrm{ibs}} = 3 \times 10^{19} \, \mathrm{m^{-3}}$, $D_\perp = 0.5 \, \mathrm{m^2 \, s^{-1}}$, $\chi_\perp = 1.5 D_\perp$, $P_{\mathrm{in}} = 5 \, \mathrm{MW}$, with $\Gamma_C = 0.04 \Gamma_H$ as a carbon source is analyzed. The resulting radiated power fraction is low, with $f_{\mathrm{rad}} = 15\%$. The distributions of the carbon radiation, the main ion density, the $\mathrm{C^{3+}}$ density (the main radiating species), and the parallel main ion flow velocity $v_\parallel$ at the horizontal target are plotted for a toroidal cross section $\varphi = 10°$ in figure 10. The plot of the carbon radiation, figure 10(*a*), indicates that there are two radiation zones in this simulation: one located at the plasma strike-line (in low iota the strike-line is located on the opposite side of the island as compared to the standard configuration plotted in figure 9) and one near the island O-point.

(a)

(b)

(c)

**Figure 9.** (*a*) The carbon radiation pattern at $f_{\rm rad} = 60\%$ for the standard configuration under standard anomalous transport assumptions, (*b*) with $\chi_\perp = 10\,{\rm m}^2\,{\rm s}^{-1}$, and (*c*) under standard anomalous transport assumptions, but with control coil current $I_{\rm cc} = -1\,{\rm kA}$.



(a)

(b)

(c)

(d)
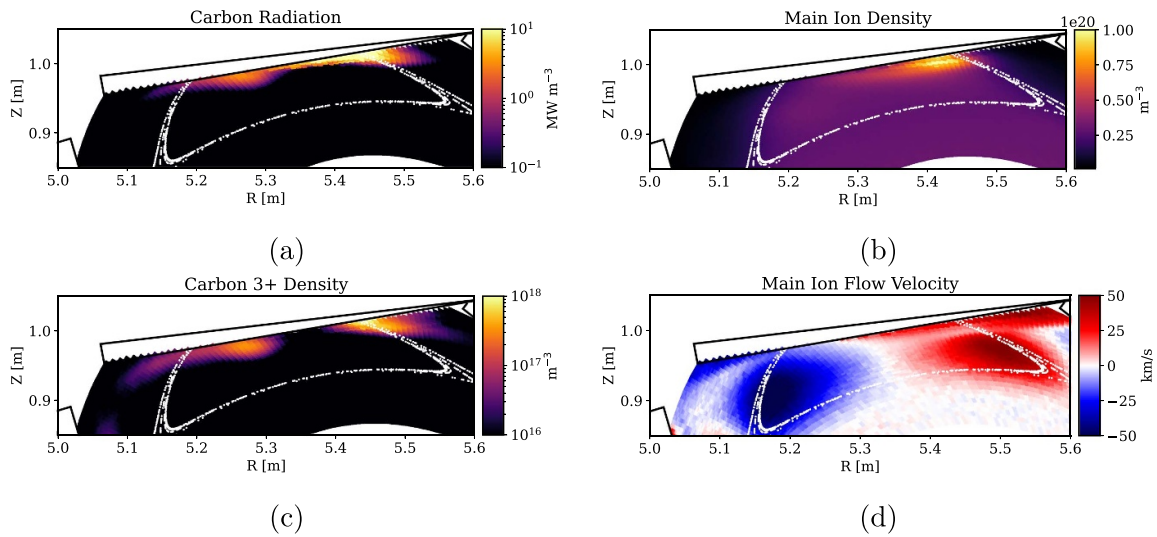
**Figure 10.** (*a*) The carbon radiation, (*b*) the main ion density, (*c*) the C$^{3+}$ density, and the parallel main ion flow velocity $v_\parallel$ distributions at a toroidal angle $\varphi = 10°$, for a simulation $n_{\rm ibs} = 3 \times 10^{19}\,{\rm m}^{-3}$, $P_{\rm in} = 5\,{\rm MW}$ and $\Gamma_C = 0.04\Gamma_{\rm rec}$.

More accurately, the 'O-point' radiation referred to in this paper actually always occurs at a location of parallel flow stagnation (where $v_\parallel = 0$, plotted in figure 10(*d*)), which is not necessarily at the exact magnetic O-point of the island and also extends radially across the island. In this simulation, the main ion density plotted in figure 10(*b*) shows no peak at the flow stagnation region—indicating that the radiation is not caused by an 'accumulation' of density. Rather, it is an increase in the density of the radiating species, C$^{3+}$, plotted in figure 10(*c*), which appears to cause the peak in radiation near the flow stagnation region. As discussed in [14], long impurity dwell times result in the C$^{3+}$ accumulation in this area.

In this simulation at low $f_{\rm rad}$, it appears as though the localized C$^{3+}$ density first triggers the O-point radiation discussed in sections 3 and 5, since $P_{\rm rad} \propto n_{\rm imp}n_{\rm e}$. However, it has not

been ruled out that the main ion sources (neutrals) may also contribute to the initialization of the radiation condensation at the flow stagnation region. To assess the effect of ionization, the impurity radiation fraction was increased to $f_{\rm rad} = 60\%$ for the simulation described above. However, this new plasma solution was iterated without including Eirene, thus keeping the particle and energy sources from the neutrals constant. As a comparison, a 2nd simulation that includes the iteration with Eirene was performed. The resulting carbon radiation and main ion density distributions for both simulations at $\varphi = 10°$ are plotted in figure 11.

Radiation condensation at the island O-point occurs both with and without iterating the plasma solution with Eirene. Figure 11(*a*) visualizes the carbon radiation pattern without iterating Eirene, while figure 11(*c*) contains a plot of the
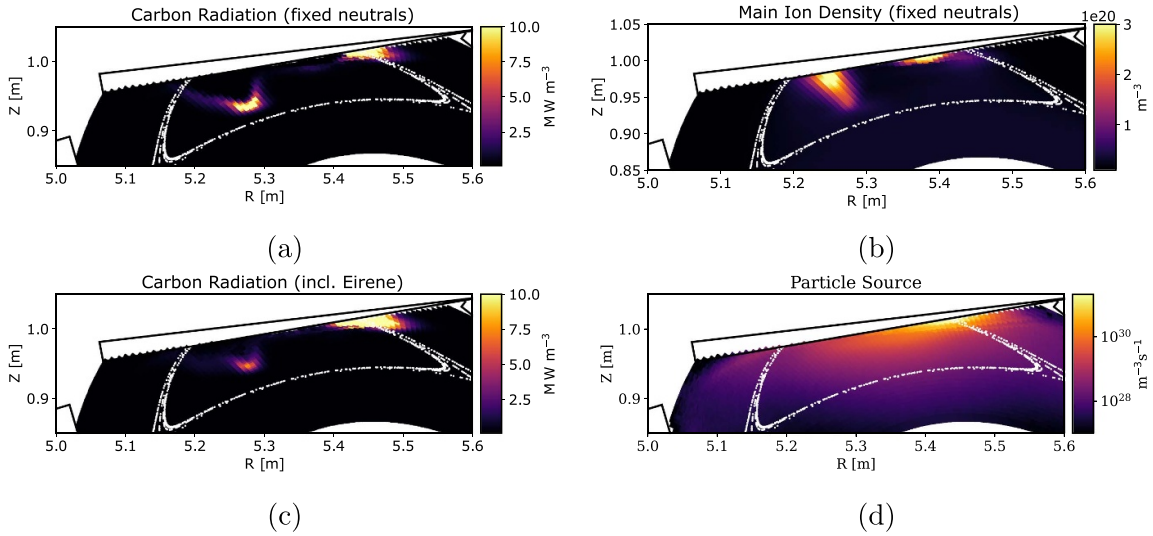
**Figure 11.** (*a*) The total carbon radiation, (*b*) main ion density distribution and (*d*) the main ion particle source at toroidal angle $\varphi = 10°$ for the same neutral particle and energy sources as in the simulation described in figure 8, but with the impurity radiation fraction increased to $f_{rad} = 60\%$. As comparison, a simulation with identical input parameters is performed, but with evolving the neutral particle and energy sources. The corresponding carbon radiation distribution at toroidal angle $\varphi = 10°$ is plotted in (*c*).

carbon radiation pattern with iterating Eirene. The magnitude of the radiation at the O-point in figure 11(*a*) is much larger than that of the radiation when including the iteration with Eirene. This indicates that the neutrals have an important role in the radiation itself, though in this case showing an opposite tendency for radiation condensation at the O-point. The large accumulation of density behind the O-point radiation condensation zone without iterating Eirene (figure 11(*b*)), arises partially because the ionization sources are still localized to the target in this simulation, but also partially because the electron temperature is extremely low in this area (~1 eV). The accumulation of density here attempts to equilibrate the pressure along the field line, resulting in the large build-up of density in the low temperature region. In contrast, the ionization source, plotted in figure 11(*d*), shows no distinct feature in this area. From the above results, it appears as though the impurity accumulation at the O-point could be a decisive factor in initializing the radiation condensation in this location. However, based on these results alone (at low plasma density) the role of the neutrals generally in all plasma conditions remains inconclusive.

### 6.2. Solution stability

This work primarily focuses on the geometrical differences in the island leading to the starkly contrasting radiation patterns between the low iota and standard magnetic field configurations. However, a short remark is made here regarding the numerical stability of the EMC3-Eirene simulations in low iota, in light of the experimental observation that the detachment in low iota appears unstable (section 3). Numerically, it was seen that at very high radiation fractions ($f_{rad} \geqslant 90\%$), a self-consistent solution could not be found with EMC3-Eirene.

The exact reason why the code cannot find a self-consistent solution is relegated to future work. While numerical effects

cannot be ruled out, the coincidental experimental observation of the oscillatory radiation behavior at high $f_{rad}$ could indicate that this numerical instability arises from physics effects. One possible cause of the solution instability has been recently published in [33], where simplified impurity transport modeling was used to obtain stable converged solutions at high radiated power fraction. Using these results, a radiation bifurcation was found in the simulations. Future work is required to understand if this radiation bifurcation can also be seen experimentally.

### 6.3. Effects of impurity species

The strong radiation condensation at the island O-point described in this paper occurs for carbon impurities, where the most efficient radiation takes place at low electron temperature ( $<10$ eV). The radiation starts near the target, where the impurities accumulate near the flow stagnation region. However, the radiation characteristics may change depending on the main radiating species in the plasma. In particular, species such as neon, which radiates at higher electron temperatures (see e.g. figure 3(*a*) of [34]) and has a longer ionization mean free path may show different transport/radiation characteristics. That neon may behave differently to carbon is also motivated by experimental observations: Experimentally, as discussed in section 3, and shown in red in figure 3, it was observed that neon seeding provided a larger range of controllable radiated power fraction before the discharge ended in radiative collapse. In fact, it is not yet clear from the experimental data if the neon-seeded detachment discharges are actually unstable. The radiative collapse of program 20230125.43 in figure 3 could also be the result of over-seeding, since the neon puffs were programmed feed-forward. Additionally, other experimental devices have seen significant differences in the detachment behavior depending
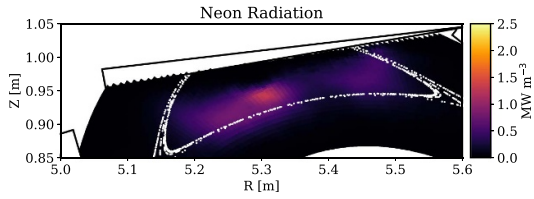
**Figure 12.** The neon impurity radiation at toroidal angle $\varphi = 10°$.

on the impurity species. For example, modeling and experimental work at LHD have indicated that neon-seeded detachment results in more homogenous unloading of the particle flux on the divertor targets in the toroidal direction as compared to nitrogen-seeded detachment [35]. However, the main driving force between the differences in neon and nitrogen seeded detachment cases in LHD was determined to be the low recycling of nitrogen from the seeding valves. In our simulations, carbon is treated as a sputtered impurity and therefore does exhibit high localization of the source. On the other hand, previous experiments on W7-X in the standard configuration for both neon-seeded and nitrogen-seeded detachment [29] and intrinsic carbon detachment [1] have seen toroidally homogenous unloading of the heat flux from the divertor target plates, even though the radiation characteristics between species were different. Therefore, we will briefly touch on the differences between neon and carbon radiation distributions in the low iota configuration using EMC3-Eirene simulations.

A simulation was performed where $n_{ibs} = 5 \times 10^{19}\,\text{m}^{-3}$, $D_\perp = 0.5\,\text{m}^2\,\text{s}^{-1}$, $\chi_\perp = 1.5 D_\perp$, and $f_{\text{rad}} = 60\%$ coming purely from neon impurities ($E_0 = 0.03$ eV, with particles started in the same distribution as the main ion recycling flux). The neon radiation distribution is plotted in figure 12. In contrast to the carbon radiation distribution, which shows strong radiation condensation near the island O-points, the neon radiation distribution is much more evenly distributed throughout the island. However, the basic features of the neon radiation do remain similar to carbon: there is a (in the case of neon, small) peak of the radiation between the island X-points, with no evidence of radiation condensation at the X-point itself.

The toroidal variation of the neon radiation is also smaller than that of the carbon radiation simulations, which is in agreement with the more upstream localization of the neon radiation. The sum of the radiated power for each toroidal angle in the simulation is plotted in figure 13 for carbon (black) and neon (red) for otherwise the same input plasma conditions ($P_{\text{in}} = 5\,\text{MW}$, $n_{\text{e,s}} = 5 \times 10^{19}\,\text{m}^{-3}$, and $f_{\text{rad}} = 60\%$). It is left to future work whether this more evenly distributed band of radiation near the LCFS is responsible for the improved controllability of neon-seeded detachment experimentally in the low iota configuration.

## 7. Conclusions

The characteristics of the radiation pattern in the low iota configuration has been studied both in experiment and using the EMC3-Eirene code. Both experimentally and numerically, radiation near the 'O-point' region (in reality at the parallel
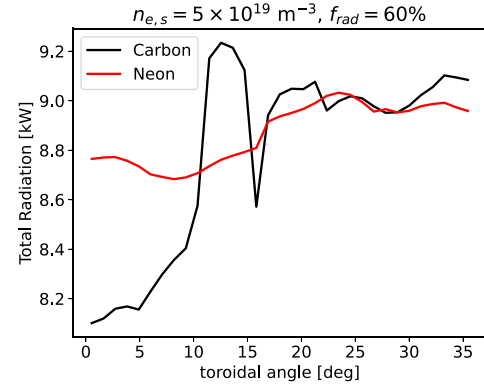


**Figure 13.** The toroidal distribution of the radiation at $n_{\text{e,s}} = 5 \times 10^{19}\,\text{m}^{-3}$, $f_{\text{rad}} = 60\%$ for a simulation using pure carbon radiation (black) versus neon radiation (red). The toroidal variation of the neon radiation is smaller than that of carbon.

flow stagnation region) is observed for intrinsic carbon impurity radiation. This localized O-point radiation is seen both in the bolometer tomographic reconstructions as well as visible spectroscopy. Experimentally, a significant up/down asymmetry exists in the radiation pattern which is currently not able to be captured in the simulation. It is hypothesized that this feature is an effect of physics not yet taken into account in the code (e.g. drifts). Additionally, although the exact radiation distribution in the simulation is sensitive to the choice of anomalous cross-field transport assumptions, the localized O-point radiation in front of the horizontal target plate is robust across many different choices of cross-field transport coefficients. Therefore, it was possible to investigate the details and cause of this radiation pattern using the EMC3-Eirene code.

The simulation results prove that it is the increased weight of perpendicular heat transport that results in the radiation condensation near the island O-point region. Numerically, configurations that normally show X-point dominated radiation condensation (e.g. the standard configuration), can be modified geometrically (via the use of island control coils) to increase the weight of perpendicular transport. In simulations where this is performed, the X-point radiation condensation disappears and the O-point radiation condensation is recovered. This numerical prediction is planned to be tested experimentally in the next operational campaign (preliminary indications from a single experiment in the last campaign show promise, but are as yet inconclusive).

The simulation and experimental results also show that the O-point radiation is not a continuous band in all islands, but is locally restricted to islands that are in close magnetic connection to the divertor target. Simulation results indicate that at low plasma density local impurity accumulation at the island O-point may be responsible for the initial radiation condensation, however this may not hold true universally. Importantly, it is likely the case that local impurity and/or ionization sources near the divertor target plate play a crucial role in the formation of the O-point radiation.

Simulations performed with neon radiation show much more evenly distributed radiation patterns. The more broadly

distributed radiation is likely a result of the different radiative characteristics of neon, which radiates at higher temperatures than carbon [34]. Thus, EMC3-Eirene simulations show that the majority of the heat is dissipated near the LCFS. However, the basic features of the neon radiation are similar to those of carbon: a peak of radiation is seen between the island X-points, with no radiation condensation at the island X-point. The lack of X-point radiation could be caused by insufficient heat transport to this region due to the increased weight of perpendicular heat flux into the island, but could also be due to source effects (for both the neutrals and impurities). There remains future work to determine whether the more evenly distributed radiation pattern from neon seeding provides better detachment controllability compared to carbon or nitrogen.

These results provide further evidence of the high importance of the internal island field line pitch on the island divertor performance, complementing the results found in previous work (e.g. [4, 8–10]). Although the localized O-point radiation is likely not a desirable feature for a future stellarator island divertor reactor, it does provide further evidence that a larger weight of parallel transport is desired for island divertor performance. Possible future work would be to further modify the island geometry to a very large internal island field line pitch, to determine limits and a possible optimum Θ for a stellarator island divertor.

## Acknowledgments

## ORCID iDs

V.R. Winters ● https://orcid.org/0000-0001-8108-7774
F. Reimold ● https://orcid.org/0000-0003-4251-7924
Y. Feng ● https://orcid.org/0000-0002-3846-4279
D. Zhang ● https://orcid.org/0000-0002-5800-4907
V. Perseo ● https://orcid.org/0000-0001-8473-9002
E.R. Flom ● https://orcid.org/0000-0002-9284-9380
D.M. Kriete ● https://orcid.org/0000-0002-3657-2911
G. Partesotti ● https://orcid.org/0009-0008-9465-7885
M. Jakubowski ● https://orcid.org/0000-0002-6557-3497
R. König ● https://orcid.org/0000-0002-4772-0051
M. Krychowiak ● https://orcid.org/0009-0001-4141-5558
K.J. Brunner ● https://orcid.org/0000-0002-0974-0457
J. Knauer ● https://orcid.org/0000-0001-7359-6472
K. Rahbarnia ● https://orcid.org/0000-0002-5550-1801

## References

[1] Feng Y. *et al* 2021 *Nucl. Fusion* **61** 086012
[2] Schmitz O. *et al* 2021 *Nucl. Fusion* **61** 016026
[3] Jakubowski M. *et al* 2021 *Nucl. Fusion* **61** 106003
[4] Feng Y. *et al* 2005 *Nucl. Fusion* **45** 89
[5] Zhang D. *et al* 2021 *Nucl. Fusion* **61** 116043
[6] Feng Y. *et al* 2014 *Contrib. Plasma Phys.* **54** 426–31
[7] Geiger J. *et al* 2015 *Plasma Phys. Control. Fusion* **57** 014004
[8] Feng Y. *et al* 2011 *Plasma Phys. Control. Fusion* **53** 024009
[9] Feng Y. *et al* 2006 *Nucl. Fusion* **46** 807
[10] Feng Y. 2022 *Plasma Phys. Control. Fusion* **64** 125012
[11] Reimold F. *et al* 2020 *28th IAEA Fusion Energy Conf.* (*Nice, FR (Virtual)*, *10–15 May 2021*) p EX/6-15 (available at: https://conferences.iaea.org/event/214/contributions/17514/)
[12] Grigull P. *et al* 2001 *Plasma Phys. Control. Fusion* **43** A175
[13] Kobayashi M. *et al* 2007 *J. Nucl. Mater.* **363–365** 294–300
[14] Winters V.R. *et al* 2024 *Nucl. Fusion* **64** 056042
[15] Brunner K.J. *et al* 2018 *JINST* **13** 09002
[16] Rahbarnia K. *et al* 2018 *Nucl. Fusion* **58** 096010
[17] Sereda S. *et al* 2020 *Nucl. Fusion* **60** 086007
[18] Hammond K.C. *et al* 2019 *Plasma Phys. Control. Fusion* **61** 125001
[19] Kriete D.M. *et al* 2023 *Nucl. Fusion* **63** 026022
[20] Perseo V. *et al* 2020 *Rev. Sci. Instrum.* **91** 013501
[21] Barbui T. *et al* 2019 *JINST* **14** C07014
[22] Feng Y. *et al* 2017 *Plasma. Phys. Control. Fusion* **59** 034006
[23] Reiter D. *et al* 2005 *Fusion Sci. Technol.* **47** 172–86
[24] Xu S. *et al* 2023 *Nucl. Fusion* **63** 066005
[25] Lazerson S. *et al* 2018 *Plasma Phys. Control. Fusion* **60** 124002
[26] Killer C. *et al* 2021 *Nucl. Fusion* **61** 096038
[27] Bold D. *et al* 2022 *Nucl. Fusion* **62** 106011
[28] Feng Y. *et al* 2021 *Nucl. Fusion* **61** 106018
[29] Effenberg F. *et al* 2019 *Nucl. Fusion* **59** 106020
[30] Frerichs H. *et al* 2016 *Rev. Sci. Instrum.* **87** 11D441
[31] Peterson B.J. *et al* 2021 *Nucl. Mater. Energy* **26** 100848
[32] Winters V.R. *et al* 2021 *Plasma Phys. Control. Fusion* **63** 045016
[33] Feng Y. *et al* 2024 *Nucl. Fusion* **64** 086027
[34] Casali L. *et al* 2022 *Nucl. Fusion* **62** 026021
[35] Kawamura G. *et al* 2018 *Plasma. Phys. Control. Fusion* **60** 084005